Coupled Dynamics of Material Delivery and Robotic Manipulator Axes in Endoscopic Additive Manufacturing

Andrej Simeunovic, Student Member and David J. Hoelzle, Member

Abstract—Tissue engineering (TE) has seen success in recapitulating the natural function of a variety of simple tissues in the laboratory setting. One barrier to increased clinical translation of tissue constructs is morbidities caused by open surgeries currently needed for their delivery into the body. Advanced robotics and control allow for new tools and manufacturing capabilities that can accelerate the clinical viability of existing forms of TE today. One such tool, an intracorporeal, additive manufacturing (AM) based TE fabrication system in an endoscopic form factor, the Endo AM system, allows for the fabrication of TE constructs inside the body in a minimallyinvasive manner. The Endo AM system consists of a 9-joint robotic manipulator and a direct-write (DW) AM extruder, leading to complex flow and positioning dynamics. Here we describe and explore the dynamics of the Endo AM system in simulation, with a focus on studying the coupling of dynamic positioning and material delivery axes.

I. INTRODUCTION

The past two decades have seen significant developments in the field of additive manufacturing (AM) based tissue engineering (TE). However, as many in the field have noted [1]–[5], the difficulty of producing natural and synthetic tissues to recapitulate natural function has slowed translation of laboratory successes to the clinical setting. There are several fundamental technical challenges to be overcome to produce complex tissues in the clinical setting, a key example being neo-vascularization (the new formation of blood vessels) [6], [7]. Simpler tissues have been more successful as a result.

An example of a simple construct that is possible today and primed for clinical translation is a hydrogel sheet with embedded angiogenic growth factors (promoters of vascularization) [8]. This tissue construct is applicable to a wide array of wound healing applications, such as oncological resections, where large tissue damage is caused by the surgery. However, delivering this construct into the body requires *ex vivo* fabrication followed by an invasive transplant procedure, which causes large tissue damage and extensive morbidities. While injectable formulations of hydrogels are one potential solution and have shown promise for simple indications [9]–[12], an endoscopic fabrication system is required to directly build structured TE constructs intracorporeally (inside the body) without invasive surgeries. As a

Manuscript received September 26, 2018; accepted January 27, 2019. Manuscript received in final form March 13, 2019.

Support for this research was provided in part by NSF CAREER Award CMMI 1708819 and NSF GRFP Award DGE 1343012.

The authors are with the Department of Mechanical and Aerospace Engineering, The Ohio State University, Columbus, OH 43210 USA (e-mail: simeunovic.1@osu.edu; hoelzle.1@osu.edu).

result, we are currently investigating robotic-assisted surgery (RAS) [13] AM architectures to develop systems capable of intracorporeal fabrication. Here we present a simulation study of an example system that meets these requirements. For shorthand, we call this system the Endo AM system, and the material delivery portion of the system, the Endo AM instrument.

The Endo AM system is composed of: 1) a 9-degree of freedom (DOF) open serial kinematic chain RAS arm based on the da Vinci Xi system (Fig. 1a), termed the endoscopic arm, and 2) a positive-displacement direct-write (DW) microextrusion tool (Fig. 1b), termed the microextrusion instrument. The large number of joints are required to overcome kinematic constraints associated with maintaining a fixed fulcrum point at the entry point into the body, called a remote center of motion (RCM), midway through the kinematic chain [14]; the RCM demarcates joints external (extracorporeal) and internal (intracorporeal) to the body (Fig. 1c). Positive displacement DW is an AM method whereby build material is extruded through a nozzle by a mechanical plunger as the nozzle moves across a printing platform [15]. DW operates by leveraging material properties of yield-pseudoplastic (YPF) build materials (inset of Fig. 1b), which hold their shape when not in shear, meaning extruded material supports itself. The microextrusion instrument in Endo AM differs from standard DW extruders in that its design matches the long (~500 mm), slender (~\@8 mm) form factor of typical RAS instruments and articulates along three orthogonal joints, which correspond to the last three joints of the system (inset of Fig. 1c). These three joints are cable driven by motors external to the body that reside near the 6th joint of the system; the material reservoir is located at this same extracorporeal position.

Dynamics and control in Endo AM are challenging due to the flow dynamics of the microextrusion instrument and the dynamic coupling between the endoscopic arm and microextrusion instrument subsystems. As shown in our previous work [16], [17], DW extrusion systems have inherent material metering challenges due to capacitive and resistive fluid dynamics (Fig. 1d). Unlike traditional robotic and DW systems, in Endo AM robot and flow dynamics are coupled; build material flowing through the microextrusion instrument causes disturbances to end-effector positioning. Individually, dynamics and control of serial kinematic manipulators [18]–[20] and YPF systems [21] are well understood. However, complete and accurate models of the unique dynamics of Endo AM are needed for use in dynamic simulations, control synthesis, and model-based controllers [22].

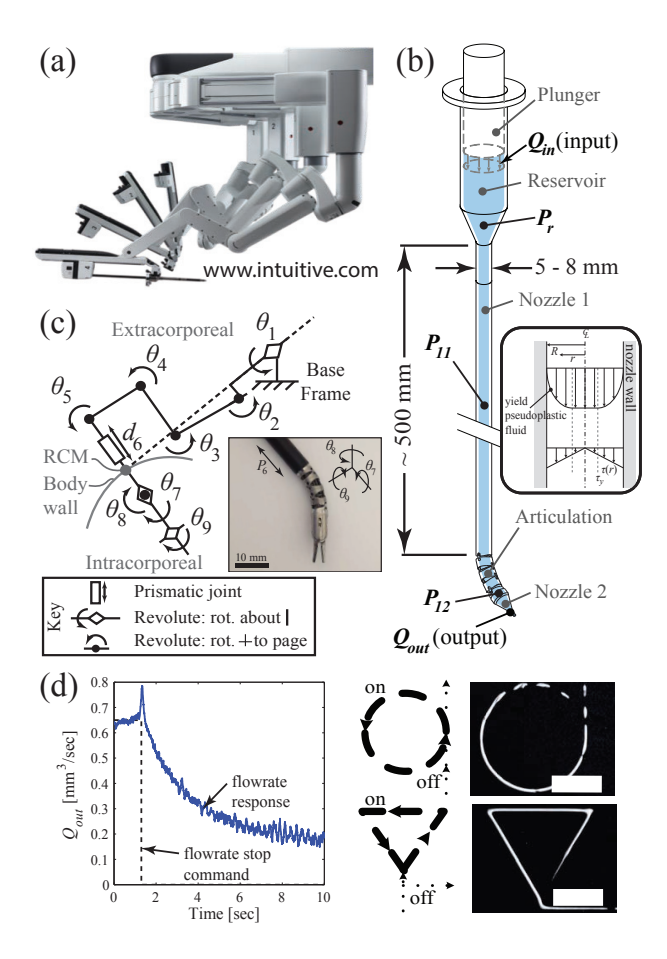


Fig. 1. Overview of Endo AM system and challenges. (a) Example endoscopic RAS system: da Vinci Xi. (b) Schematic of Endo AM microextrusion instrument. Inset: Build material in DW is yield-pseudoplastic fluid. (c) Schematic of Endo AM system joints, highlighting revolute and prismatic joints, RCM, and intra- and extra- corporeal joints. Inset: Close-up of traditional RAS instrument with three revolute axes highlighted. Endo AM microextrusion instrument articulates along these same three axes. (d) Capacitive fluid dynamics in DW result in charging and discharging phenomena during transient flows [16]. Printing simple shapes with DW demonstrates poor transient flow control [17] that leads to manufacturing inaccuracies. Scale bars are 5 mm.

The goal of this work is to synthesis a model of the coupled Endo AM dynamics and study them through simulation. We limit our scope to developing and studying the coupled dynamic model, with control design planned for future work. The remainder of the paper is outlined as follows: Section II details the system and model synthesis; Section III presents the simulation study; Section IV discusses the results, conclusions, and future work.

II. SYSTEM DESCRIPTION AND MODEL

We assume an adiabatic process with compressible, laminar, steady flow dominated by viscous forces. We assume all robotic links are rigid and for intracorporeal joints $\theta_7 - \theta_9$, the small masses, low friction coefficients, and low gear ratios render inertial and friction effects negligible. In the microextrusion instrument, we assume negligible fluidic resistance for the reservoir due to its large radius and negligible fluidic capacitance for nozzle 2 due to its small volume. In

the coupled model, we neglect disturbance effects due to the net rate of momentum flow through the microextrusion instrument as forces due to momentum flux are $O(10^{-8})$, ten orders of magnitude less than those of pressure disturbances.

This section describes the model for the endoscopic arm (Section II-A), the microextrusion instrument (Section II-B), and the coupling between the two (Section II-C). Throughout, we will denote joint torques by vector-valued variable τ and fluid shear stress by scalar τ as is the convention in their respective communities. When discussing robot joints, R and P refer to revolute and prismatic joints, respectively.

A. Endoscopic Arm

The endoscopic arm is modeled after the da Vinci Xi (Intuitive Surgical, Sunnyvale, CA) (Fig. 1a), a RAS system which has 14-joint (11R, 3P) manipulators. Of these 14-joints, only 9 are active during surgical procedures, with the remaining 5 used for positioning of the base frame of the active portion of the manipulator and its RCM. Likewise, Endo AM has 9 joints (8R, 1P) and a 5-DOF positioning base that defines the base frame of the system and the system's RCM prior to operation. The 6 extracorporeal DOFs (θ_1 – d_6) are large (~1200 mm² cross-section, >250 mm long, 3-5 kg), requiring torques up to 75 Nm to drive. Conversely, the 3 intracorporeal DOFs (θ_7 – θ_9) are small - the entire subsystem defining these joints is 200 g - requiring torques from inertial effects on the order of μ Nm.

Forward kinematics of the Endo AM system follow standard conventions of transformation matrices [18] based on Denavit-Hartenberg parameters (D-H, Tables I and II) and are omitted here for brevity. The inverse kinematics are more complex. Typically, a highly kinematically overdefined serial system has no closed-form inverse kinematic solution. However, the RCM must be maintain a fixed position relative to the base frame, leading to two positional constraints. We impose a third, artificial constraint to break the problem into two tractable serial problems for the extra- and intracorporeal joints. For the intracorporeal joints, the RCM frame is the base frame and two virtual revolute joints (γ , λ) provide the rotational DOFs of the extracorporeal joints.

Endo AM dynamics are a function of torques due to manipulator motions (τ_m) , apparent inertias (τ_{rot}) , springs (τ_{sp}) , and disturbances (τ_{dis}) , with generalized joint torques

$$\tau(t) = \tau_{\mathbf{m}}(t) + \tau_{\mathbf{rot}}(t) + \tau_{\mathbf{sp}}(t) + \tau_{\mathbf{dis}}(t).$$

Torques due to apparent inertias arise in the extracorporeal joints as a consequence of minimizing size while maintaining high torque output - large gear ratios are required for the extracorporeal joints resulting in high angular velocity of the joint rotors and appreciable joint torques due to apparent inertia [20]. Spring torques are present in intracorporeal joints $\theta_7 - \theta_9$ (inset of Fig. 1c) as spring dynamics dominate due to their cable-driven design. Disturbance torques arise due to the pressurizing of the microextrusion instrument and are described in Section II-C.

 $\label{eq:table_interpolation} \mbox{TABLE I}$ D-H Parameters, intracorporeal DOFs

i	α_{i-1}	a_{i-1}	d_i	θ_i
γ	0	0	0	θ_{γ}
λ	-90°	0	0	$ heta_\lambda$
6	90°	0	d_6	0
7	0	0	d_7	θ_7
8	-90°	0	0	θ_8 -90°
9	90°	a_8	0	θ_9
TABLE II				

D-H PARAMETERS, EXTRACORPOREAL DOFS

i	α_{i-1}	a_{i-1}	d_i	θ_i
1	0	0	0	θ_1
2	-90°	a_1	0	θ_2
3	0	a_2	0	θ_3
4	0	a_3	0	θ_4
5	0	a_4	0	θ_5

The dynamics due to manipulator motions are represented using the Euler-Lagrange formulation [19]

$$\boldsymbol{\tau}_{\mathbf{m}}(t) = \mathbf{D}(\boldsymbol{\theta}(t)) \, \ddot{\boldsymbol{\theta}}(t) + \mathbf{c}(\boldsymbol{\theta}(t), \dot{\boldsymbol{\theta}}(t)) + \mathbf{g}(\boldsymbol{\theta}(t)) + \mathbf{f}(\dot{\boldsymbol{\theta}}(t))$$

where θ , $\dot{\theta}$, $\ddot{\theta} \in \mathbb{R}^{9 \times 1}$ are the joint position, velocity, and acceleration vectors, respectively, $\mathbf{D} \in \mathbb{R}^{9 \times 9}$ is the inertia matrix, and \mathbf{c} , \mathbf{g} , $\mathbf{f} \in \mathbb{R}^{9 \times 1}$ are vectors of Coriolis/centripetal, gravity, and friction effects, respectively. We adopt a friction model that includes Coulomb and viscous effects [18]

$$\mathbf{f}\left(\dot{\boldsymbol{\theta}}\left(t\right)\right) = \mathbf{F_c} \operatorname{sign}\left(\dot{\boldsymbol{\theta}}\left(t\right)\right) + \mathbf{F_v}\dot{\boldsymbol{\theta}}\left(t\right)$$

where $\mathbf{F_c}$, $\mathbf{F_v} \in \mathbb{R}^{9x9}$ are diagonal matrices of Coulomb and viscous friction parameters, respectively.

Torques due to apparent inertias are given by

$$\tau_{\text{rot}}(t) = \mathbf{G}^2 \mathbf{I}_{\text{rot}} \ddot{\boldsymbol{\theta}}_{1-6}(t)$$

where \mathbf{G} , $\mathbf{I_{rot}} \in \mathbb{R}^{6\times 6}$ are diagonal matrices of gear ratios and rotor static inertia terms about the respective joint axis, respectively, for $\theta_1 - d_6$; $\ddot{\theta}_{1-6}(t) \in \mathbb{R}^{6\times 1}$ is the joint acceleration vector for $\theta_1 - d_6$. To make $\boldsymbol{\tau_{rot}} \in \mathbb{R}^{9\times 1}$, we set the three entries corresponding to $\theta_7 - \theta_9$ to zero.

For simplicity we model the cables in $\theta_7 - \theta_9$ as linear springs and the resulting spring torques are given by

$$\tau_{\rm sp}(t) = \mathbf{K}\theta_{7-9}(t)$$

where $\mathbf{K} \in \mathbb{R}^{3\times 3}$ is the diagonal matrix of spring constants $\mathbf{K} = \operatorname{diag}(K_7, K_8, K_9)$, and $\theta_{7-9}(t) \in \mathbb{R}^{3\times 1}$ is the joint position vector for $\theta_7 - \theta_9$. To make $\boldsymbol{\tau}_{\mathbf{sp}} \in \mathbb{R}^{9\times 1}$, we set the six entries corresponding to $\theta_1 - d_6$ to zero.

B. Microextrusion Instrument

The microextrusion instrument has fluidic capacitance and resistance (Fig. 2a). Capacitors are functions of material bulk modulus, β , and fluid volume. Resistors are nonlinear functions of geometric factors, pressure drop (ΔP), and rheology parameters of the fluid (Eqn. 1) [21]. The reservoir (Fig. 2b) has appreciable capacitance (C_r) due to a large volume. Nozzle 1 has appreciable capacitance (C_1) and resistance due to a large volume and small radius. Nozzle 2 has appreciable resistance (R_2) due to a small radius. For simplicity, we model C_1 acting at the geometric center of nozzle 1 and model the first and second halves of nozzle 1 as separate resistors R_{11} and R_{12} .

The pressures in the reservoir and nozzle 1 are defined as

$$\dot{P}_{r} = \frac{\beta}{V_{0,r} - V_{in}} (Q_{in} - Q')$$
$$\dot{P}_{1} = \frac{\beta}{V_{1}} (Q' - Q_{out})$$

where $V_{0,r}$ is the initial material volume in the reservoir and V_1 is the material volume in nozzle 1. V_{in} is the input volume into the reservoir, and Q_{in} , Q', and Q_{out} , are the flow rates at the input, midpoint of nozzle 1, and output, respectively.

DW systems utilize yield-pseudoplastic fluids (YPFs) which we model with the Herschel-Bulkley constitutive equation

$$\tau = \tau_0 + m\dot{\gamma}^n$$

where, for a given shear rate $\dot{\gamma}$, the one-dimensional shear stress (along the nozzle central axis), τ , is defined by the yield stress τ_0 , the fluid consistency index m, and the flow behavior index n [21]. Dropping subscripts for generality, the flow rate of a YPF through a nozzle is given by Equation 1 where $\phi = \frac{\tau_0}{\tau_w}$ and $\tau_w = \frac{4P}{L} \frac{R}{2}$ [21]. Importantly, Q_{out} flows through both resistors \mathcal{R}_{12} and \mathcal{R}_2 , allowing us to solve for pressure P_2 as a function of the resistances and P_1 . Nominally, solving for P_2 requires the application of a nonlinear solver at each time step; to minimize the computational penalty, we linearize the resistances using operating points at steady state flow, a procedure we have previously shown has minimal accuracy penalty [16]. Then, the linearized resistances are

$$(\mathcal{R}_{12})^{-1} = \frac{\partial Q_{out,1}}{\partial (P_1 - P_2)} \Big|_{P_1 - P_2 = \bar{P}_1 - \bar{P}_2}$$
$$(\mathcal{R}_2)^{-1} = \frac{\partial Q_{out,2}}{\partial P_2} \Big|_{P_2 = \bar{P}_2}$$

and P_{12} is found with standard circuit analysis,

$$P_{12} = \left(\frac{\mathcal{R}_{12}}{\mathcal{R}_2} + 1\right)^{-1} P_{11}.$$

$$Q = \begin{cases} \pi R^3 n \left(\frac{\tau_w}{m}\right)^{1/n} (1 - \phi)^{(n+1)/n} \left[\frac{(1 - \phi)^2}{3n + 1} + \frac{2\phi(1 - \phi)}{2n + 1} + \frac{\phi^2}{n + 1} \right] & \text{for } \phi \le 1\\ 0 & \text{for } \phi > 1 \end{cases}$$
(1)

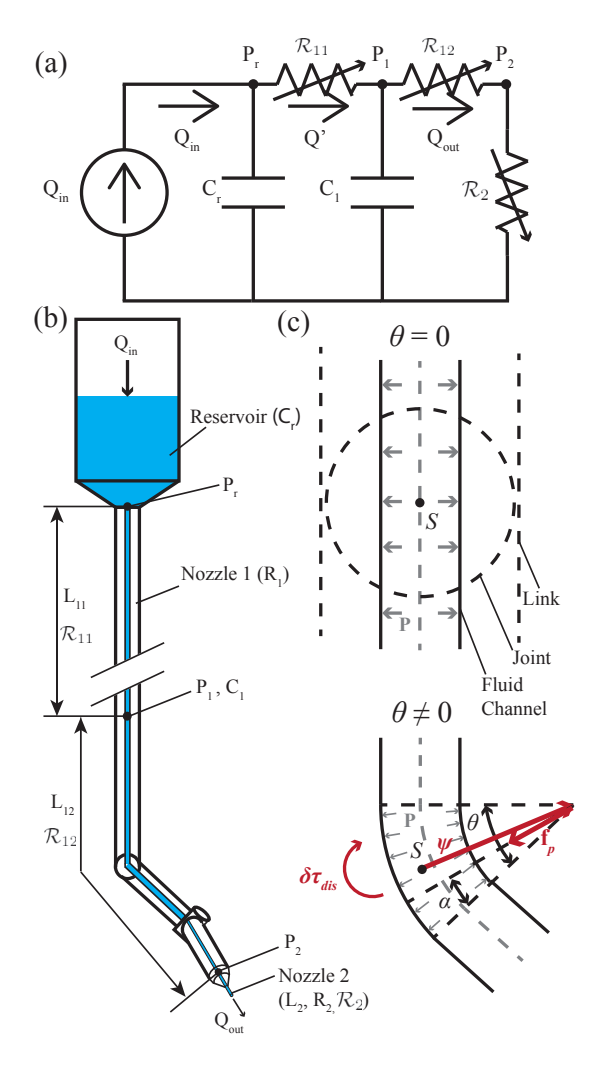


Fig. 2. Flow dynamics in microextrusion instrument. (a) Fluidic circuit of microextrusion instrument. (b) Schematic of microextrusion instrument with flow parameters highlighted. (c) Disturbance torques result from bending the pressurized microextrusion fluid channel. Disturbance torques tend to straighten the joint.

C. Coupling Between Endoscopic Arm and Microextrusion Instrument

The microextrusion instrument winds through the intracorporeal joints of the endoscopic arm, coupling the dynamics between robot and microextrusion axes, and straightens the endoscopic arm, much like a pressurized garden hose straightens during flow (Fig. 2c). More precisely, the fluid channel bends with θ_8 and θ_9 and as joint angle increases the centerline of the fluid channel bends away from the origin of the respective joint, S. The resulting differential force from internal pressure, $\mathbf{f_p}(\theta)$, causes a disturbance torque

$$\delta \tau_{\text{dis}}(\alpha, \theta) = \psi(\theta) \times f_{p}(\alpha, \theta)$$

where $\psi(\theta)$ is the position vector from S to the virtual center of curvature of the fluid channel. The disturbance torque is integrated from 0 to θ with integration parameter α to find the total disturbance torque,

$$\tau_{\text{dis}} = 4R^2 LP \left(\frac{1}{\theta} (\cos \theta - 1) + \frac{1}{2} \sin \theta \right)$$

where R and L are the radius and length of the fluid channel of the respective joint, and P is the pressure for the respective joint. The scalar total disturbance torques for θ_8 and θ_9 comprise the last two entries in the disturbance torque vector, $\tau_{\rm dis}(t)$, while all others are zero.

III. SIMULATION STUDY

For all simulation cases we simulate an end-effector trajectory corresponding to printing a hydrogel sheet in the body: a 50 mm x 50 mm raster path over a 5 mm tall spherical convex dome (Fig. 3a). We choose a stand-off height of 0.4 mm, a standard height for the selected nozzle diameter. The end-effector orientation is chosen so that the nozzle points into the dome, normal to the dome surface at each point in the path. The large values of fluidic resistance and capacitance in the microextrusion instrument lead to very long (>30 sec) rise and fall times for Q_{out} with open loop control. Therefore, we simulate a simple proportional feedback control to meet the desired reference trajectories. The simulation parameters (Tb. III) are derived from the geometry of an Endo AM system currently being made in the lab and measured fluid material properties from previous work [16].

TABLE III
SIMULATION PARAMETERS

Parameter	Symbol	Value	Units
Nozzle 1 Length	$L_{11} + L_{12}$	500	mm
Nozzle 2 Length	L_2	15	mm
Nozzle 1 Radius	R_1	1.15	mm
Nozzle 2 Radius	R_2	255	μ m
Reservoir Volume	$V_{0,r}$	2	mL
Fluid Bulk Modulus	β	56.7	MPa
Fluid Yield Stress	$ au_0$	144.43	Pa
Fluid Consistency Index	m	76.17	Pa-s ⁿ
Fluid Behavior Index	n	0.70	_

TABLE IV
SIMULATION CASES

Case	Q_{in}	$K\left[\frac{\mathrm{Nm}}{\mathrm{rad}}\right]$
I	Constant	0.249
II	Constant	0.003
III	Pulsed	0.249
IV	Pulsed	0.003

We examine two cases for the desired output flow rate, Q_{out} : one in which the output flow rate is held constant (Fig. 3b and Cases I and II in Tb. IV) and one in which the output flow rate is pulsed, as would be required to print a structure with vacancies of material in the center (Fig. 3b and Cases III and IV in Tb. IV). We examine two cases of spring stiffness based on values reported in the literature [22]: one in which the spring is appreciably stiff (Cases I and III in Tb. IV), and one in which the spring is appreciably compliant (Cases II and IV in Tb. IV). We assume $K_7 = K_8 = K_9 = K$ for all simulations.

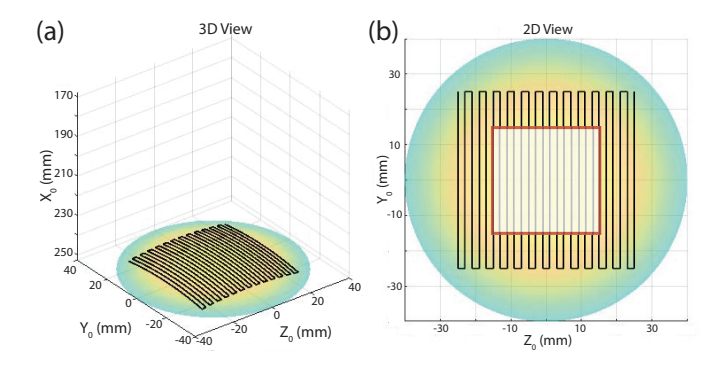


Fig. 3. End effector trajectory and flow reference signal. (a) End effector trajectory for all simulation cases. (b) For constant flow reference (Cases I, II), the entire raster path is printed. For pulsed flow reference (Cases III, IV), the square in center of the path is not printed.

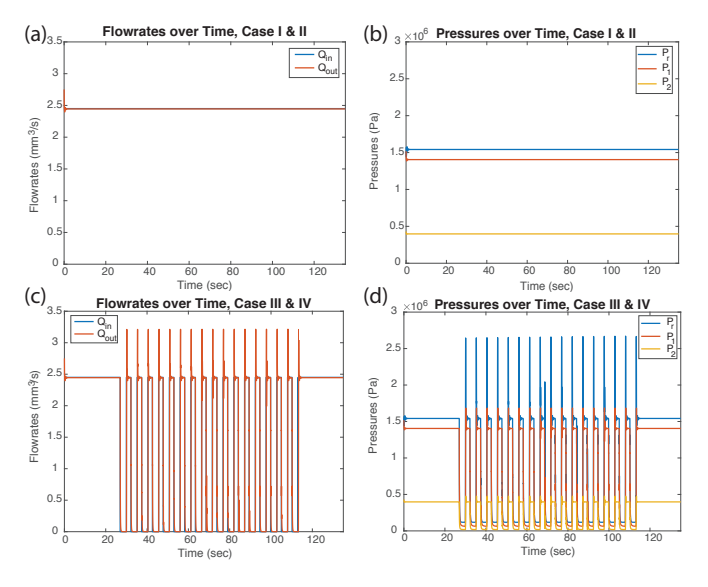


Fig. 4. Simulation results. (a,b) Flow rates and pressures over time for constant Q_{in} ; corresponds to Cases I and II. (c,d) Flow rates and pressures over time for pulsed Q_{in} ; corresponds to Cases III and IV.

For flow rate quantification, we report output Q_{out} for given reference Q_{in} over time, and pressures P_r , P_1 , and P_2 over time. With feedback controlled flow rate the primary causes of errors in deposited material on the build plate are due to nozzle position and orientation errors. As a result, we omit quantifying deposited flow errors. For nozzle position errors, we present the two-dimensional desired (no disturbance) and actual (with disturbance) nozzle position, which correspond to axes Y_0 and Z_0 in the base frame. We present errors in the stand-off height - axis X_0 in the base frame - as simple differences over time between desired and actual. Note that the Euclidean norm is not taken for stand-off errors so that positive and negative errors are representative of away from and into, respectively, the dome printing surface. We present nozzle orientation errors with Frobenius norms of the matrix at each time step.

IV. RESULTS, DISCUSSION, AND CONCLUSIONS

Spring stiffness and reference flow rate both have appreciable effects on the end-effector position and orientation;

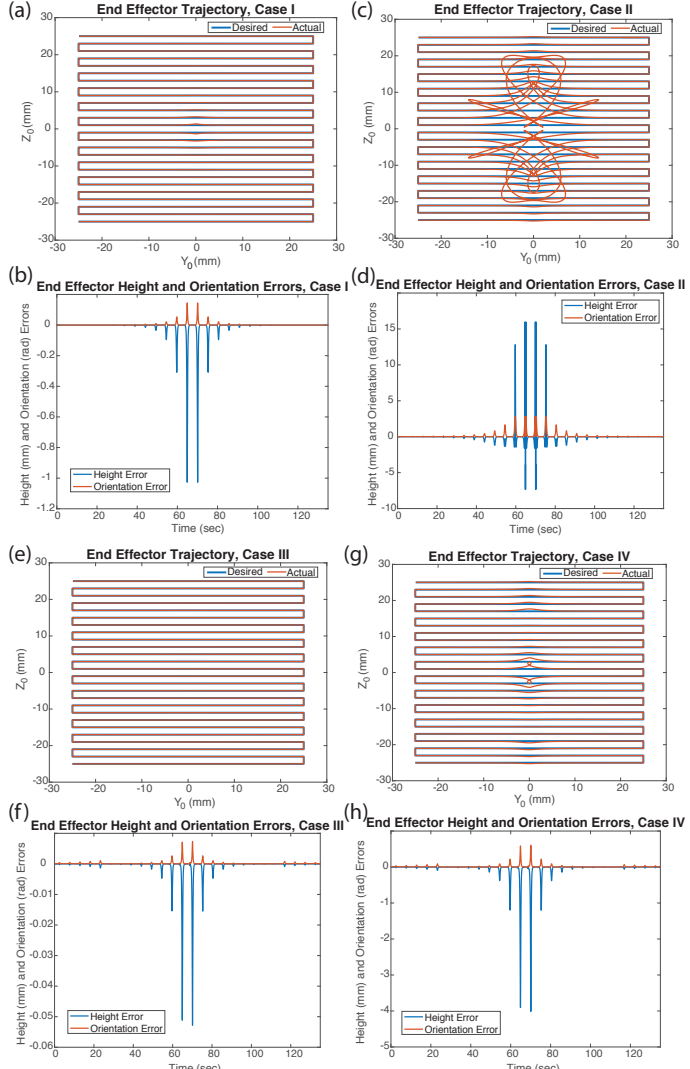


Fig. 5. Simulation positioning results: two-dimensional nozzle position (looking down at dome) of *desired* and *actual* trajectories and stand-off height and orientation error over time. (a,b) Case I. (c,d) Case II. (e,f) Case III. (g,h) Case IV.

by extension, both spring stiffness and reference flow rate impact manufacturing accuracy. Spring stiffness directly governs the magnitude of deflections of θ_8 and θ_9 . The stiff spring (Cases I and III, Figs. 5a, 5b, 5e, 5f) has smaller deflections than the compliant spring (Cases II and IV, Figs. 5c, 5d, 5g, 5h). Pulsed Q_{in} improves end-effector trajectories as seen in both the stiff (Case I: constant Q_{in} , Figs. 4a, 4b, 5a, 5b; Case III: pulsed Q_{in} , Figs. 4c, 4d, 5e, 5f) and compliant (Case II: constant Q_{in} , Figs. 4a, 4b, 5c, 5d; Case IV: pulsed Q_{in} , Figs. 4c, 4d, 5g, 5h) cases. End-effector pose is such that at the center of the path $(Y_0, Z_0 \approx 0 \text{ mm})$, joint θ_8 has a large (~ 1.3 rad) joint angle, creating a large disturbance torque, τ_{dis} , in this region of the end-effector space. At regions far from the center, joint angle is approximately 0.2 rad, and therefore subjected to minimal disturbance torque. By pulsing Q_{in} near the center of the path, the number of disturbance time steps when the nozzle is near the center is reduced, smoothing out the high-deflection regions of the end-effector trajectory. While the stiff spring configuration with pulsed flow (Case III) results in the trajectory closest to desired (Figs. 5e, 5f), the stand-off height error ($\approx 10\%$ closer to platform) is still sufficient to flatten the printed filament, appreciably impacting manufacturing accuracy. The other cases (I, II, IV) have stand-off height errors large enough to collide with the printing platform.

Additional control architectures are needed to overcome the identified system disturbances. For material metering, we implemented feedback control of flow rate directly, a control scheme that is not realizable in practice as no real-time flow rate sensors appropriate for DW exist. A more tractable approach that requires further study is the feedback control of microextrusion pressures. For robot positioning, compensation for the disturbances to θ_8 and θ_9 is required. As these disturbances are functions of flow parameters, joint trajectories, and fixed system parameters, feedforward, model-based compensation may be a viable solution.

In future work we will explore relevant sensors and control schemes to address the control needs of the robotic and microextrusion axes. Additionally, we will perform system identification studies on the da Vinci Xi EndoWrist instruments to determine realistic values for assumed system parameters and the spring constants for joints $\theta_7 - \theta_9$. This work will inform the design and construction of the Endo AM system and instrument, as the coupling of experimental data and the presented model will allow us to directly address these problematic dynamics in the design process. For example, we will be able to directly test spring constants and understand the resulting deflections, understand limits on nozzle diameters as these will drive fluidic resistances and pressure spikes, and understand regions of the joint space in which errors will be large.

In summary, we have presented and modeled the dynamics of Endo AM, a novel, surgical robotic DW AM instrument designed for minimally-invasive, intracorporeal tissue engineering. As we have shown, the flow and positioning dynamics of the system are complex and coupled, leading to control challenges in several areas. While we have identified key contributors to these challenges, more study is required to understand and control all phenomena governing the Endo AM dynamics, the details of which we have outlined in our planned future work.

ACKNOWLEDGEMENT

We wish to acknowledge our collaborators at the Ali Asghari Adib and Dr. Desmond D'Souza for their thoughtful discussions, clinical insight, access to da Vinci training systems, and continued support of the Endo AM project.

REFERENCES

- S. J. Hollister and W. L. Murphy, "Scaffold Translation: Barriers Between Concept and Clinic," *Tissue Engineering: Part B*, vol. 17, no. 6, pp. 459–474, 2011.
- [2] A. Atala, F. K. Kasper, and A. G. Mikos, "Engineering Complex Tissues," *Science Translational Medicine*, vol. 4, no. 160, pp. 160rv12, 1–10, 2012.

- [3] I. T. Ozbolat and M. Hospodiuk, "Biomaterials Current advances and future perspectives in extrusion-based bioprinting," *Biomaterials*, vol. 76, pp. 321–343, 2016.
- [4] T. Billiet, M. Vandenhaute, J. Schelfhout, S. Van Vlierberghe, and P. Dubruel, "A review of trends and limitations in hydrogel-rapid prototyping for tissue engineering," *Biomaterials*, vol. 33, no. 26, pp. 6020–6041, 2012.
- [5] F. P. W. Melchels, M. A. N. Domingos, T. J. Klein, J. Malda, P. J. Bartolo, and D. W. Hutmacher, "Additive manufacturing of tissues and organs," *Progress in Polymer Science*, vol. 37, no. 8, pp. 1079–1104, 2012.
- [6] E. C. Novosel, C. Kleinhans, and P. J. Kluger, "Vascularization is the key challenge in tissue engineering," *Advanced Drug Delivery Reviews*, vol. 63, no. 4, pp. 300–311, 2011.
- [7] H. Bae, A. S. Puranik, R. Gauvin, F. Edalat, B. Carrillo-Conde, N. A. Peppas, and A. Khademhosseini, "Building Vascular Networks," *Science Translational Medicine*, vol. 4, no. 160, pp. 160ps23, 1–5, 2012.
- [8] P. Schumann, D. Lindhorst, C. Von See, N. Menzel, A. Kampmann, F. Tavassol, H. Kokemüller, M. Rana, N. C. Gellrich, and M. Rücker, "Accelerating the early angiogenesis of tissue engineering constructs in vivo by the use of stem cells cultured in matrigel," *Journal of Biomedical Materials Research Part A*, vol. 102, no. 6, pp. 1652–1662, 2014.
- [9] C. M. Hwang, B. Ay, D. L. Kaplan, J. P. Rubin, K. G. Marra, A. Atala, J. J. Yoo, and S. J. Lee, "Assessments of injectable alginate particleembedded fibrin hydrogels for soft tissue reconstruction," *Biomedical Materials*, vol. 8, no. 1, p. 014105, 2013.
- [10] E. A. Silva and D. J. Mooney, "Spatiotemporal control of vascular endothelial growth factor delivery from injectable hydrogels enhances angiogenesis," *Journal of Thrombosis and Haemostasis*, vol. 5, no. 3, pp. 590–598, 2007.
- [11] B. K. Chan, C. C. Wippich, C. J. Wu, P. M. Sivasankar, and G. Schmidt, "Robust and Semi-Interpenetrating Hydrogels from Poly(ethylene glycol) and Collagen for Elastomeric Tissue Scaffolds," *Macromolecular Bioscience*, vol. 12, no. 11, pp. 1490–1501, 2012.
- [12] W. Zhang, X. Wang, S. Wang, J. Zhao, L. Xu, C. Zhu, D. Zeng, J. Chen, Z. Zhang, D. L. Kaplan, and X. Jiang, "The use of injectable sonication-induced silk hydrogel for VEGF 165 and BMP-2 delivery for elevation of the maxillary sinus floor," *Biomaterials*, vol. 32, no. 35, pp. 9415–9424, 2011.
- [13] G. Y. Tan, R. K. Goel, J. H. Kaouk, and A. K. Tewari, "Technological Advances in Robotic-Assisted Laparoscopic Surgery," *Urologic Clinics of North America*, vol. 36, no. 2, pp. 237–249, 2009.
- [14] G. Guthart and J. Salisbury, "The Intuitive telesurgery system: overview and application," *Proceedings of the 2000 IEEE International Conference on Robotics & Automation*, vol. 1, no. April, pp. 618–621, 2000.
- [15] J. Cesarano III, R. Segalman, and P. Calvert, "Robocasting provides moldless fabrication from slurry deposition," *Ceramic Industry*, vol. 148, no. 4, pp. 94–102, 1998.
- [16] A. Simeunovic and D. J. Hoelzle, "Nonlinear and linearized gray box models of direct-write printing dynamics," *Proceedings of the* 29th Annual International Solid Freeform Fabrication Symposium, pp. 1953–1975, 2018.
- [17] D. J. Hoelzle, A. G. Alleyne, and A. J. Wagoner Johnson, "Iterative Learning Control for Robotic Deposition Using Machine Vision," in *American Control Conference*, 2008, pp. 4541–4547.
- [18] J. J. Craig, Introduction to Robotics: Mechanics and Control, 4th ed. New York, NY: Pearson Eduction, 2018.
- [19] M. W. Spong, S. Hutchinson, and M. Vidyasagar, Robot Modeling and Control, 1st ed. Hoboken, NJ: John Wiley & Sons, 2006.
- [20] K. M. Lynch and F. C. Park, Modern Robotics: Mechanics, Planning, and Control, 1st ed. New York, NY, USA: Cambridge University Press, 2017.
- [21] R. Chhabra and J. Richardson, Non-Newtonian Flow and Applied Rheology: Engineering Applications, 2nd ed. Oxford: Elsevier Ltd, 2008
- [22] G. A. Fontanelli, F. Ficuciello, L. Villani, and B. Siciliano, "Modelling and identification of the da Vinci Research Kit robotic arms," *IEEE International Conference on Intelligent Robots and Systems*, vol. 2017–September, pp. 1464–1469, 2017.